

Glass stability (GS) of chemically complex (natural) sub-alkaline glasses

G. Iezzi^{1,2}, A.L. Elbrecht³, M. Davis³, F. Vetere⁴,
V. Misiti², S. Mollo^{5,2}, A. Cavallo^{6,2}

¹Dep. “Ingegneria & Geologia (InGeo), University G. d’Annunzio of Chieti-Pescara, Italy;

²SCHOTT North America, New York, USA;

³Department of Physics and Geology University of Perugia Italy;

⁴INGV Rome Italy;

⁵Dep. “Scienze della Terra”, University La Sapienza University of Roma, Italy.

⁶CETREMA Grosseto, Italy;

Corresponding author: Gianluca Iezzi (g.iezzi@unich.it)

Keywords: DSC, SEM, EPMA, GS (glass stability), GFA (glass-forming ability).

Abstract

Glass stability (GS) indicates the glass reluctance or ability to crystallise upon heating; it can be characterised by several methods and parameters and is frequently used to retrieve glass-forming ability (GFA) of corresponding liquids as the case with which such liquids can be made crystal free via melt-quenching. Here, GS has been determined for the first time on six sub-alkaline glasses having complex (natural) compositions, the most widespread and abundant on Earth. The two end-members are a basalt and a rhyolite, B₁₀₀ and R₁₀₀, plus intermediate compounds B₈₀R₂₀, B₆₀R₄₀, B₄₀R₆₀, B₂₀R₈₀. Each glass was heated in a differential scanning calorimetry (DSC) at a rate of 10 °C/min (600 °C/h) to measure *in-situ* T_g (glass transition), T_x (onset of crystallization) and T_m (melting) temperatures, from ambient to their *liquidus* temperatures. The *ex-situ* run-products quenched at T_m have been characterised by SEM and EPMA to quantify textures and compositions of phases, respectively.

R₁₀₀ and B₂₀R₈₀ do not show any DSC peak, whereas B₄₀R₆₀, B₆₀R₄₀, B₈₀R₂₀ and B₁₀₀ thermograms display progressively more resolvable peaks. As SiO₂ (wt.%) in the system increases from B₁₀₀ to B₄₀R₆₀, T_x linearly increases, T_m first decreases and then levels off, whereas T_g poorly changes. In agreement, R₁₀₀ and B₂₀R₈₀ run-products are completely glassy, while from B₁₀₀ to B₄₀R₆₀ the amount of glass (gl) increases from 48.5 to 97 area%, counterbalanced by a decreasing of clinopyroxene (cpx) from 47.7 to 16 area%, whereas spinel (sp) accounts of only 0.9 to 3.8 area%. Plagioclase (plg) crystallises heterogeneously on the Al₂O₃ holders only in B₁₀₀ and B₈₀R₂₀ and for distance < 100 µm from it. R₁₀₀, B₂₀R₈₀, B₄₀R₆₀ and B₆₀R₄₀ *ex-situ* glasses have chemistries very close to their starting compositions, according to the absence or scarcity of crystals formed during heating. Instead, B₁₀₀ and B₈₀R₂₀ glasses are enriched in Si, Al and Na and depleted in Fe, Mg and Ca due to internal crystallization of sp and mostly cpx. Cpx in B₁₀₀ is rich in ^{M2}Ca, ^{M1}Mg, ^{M2,M1}Fe and remarkably of ^{M1,T}Al.

K_T , K_H , K_W , K_{LL} and w_2 GS parameters increase linearly and monotonically as a function of SiO₂, with very high correlations. Moreover, T_x values and GS parameters highly correlate with GFA *via* R_c (critical cooling rate), previously determined with *ex-situ* cooling-induced experiments. Therefore, GS scales with GFA for natural silicate compositions. In addition, the *in-situ* R_c value of B₁₀₀ measured with DSC results > 45 °C/min (> 2700 °C/h), broadly corroborating the R_c of about 150 °C/min (9000 °C/h) determined *ex-situ*. In turn, relevant solidification parameters on heating or cooling can be obtained by DSC investigations also for chemically complex (natural) systems, similar to simple silicate systems. These outcomes are relevant for lavas or magmas that re-heat glass-bearing volcanic rocks, as well as for fabricate glass-ceramic materials with desirable texture and composition of phases starting from abundant and very cheap raw volcanic rocks.

Introduction

In Earth Sciences, dynamic solidification processes have been studied mainly by *ex-situ* cooling-induced ([1-11] and reference therein) and to a lesser extent by decompression-induced degassing experiments [4, 12-15], starting from a dry or volatile-bearing silicate liquid \pm crystals. The major part of these studies focus on SiO₂-poor systems, relevant for basaltic lavas and magmas, whereas more SiO₂-rich systems are by far lesser investigated [4, 6, 10-11]. Even fewer investigations are available for solidification behaviours induced by heating or re-heating on glasses, except for a few studies on basaltic to basaltic-andesite systems [16-22]. In parallel, differential scanning calorimetry (DSC) and/or differential thermal analysis (DTA) techniques are rarely applied on crystallization of liquids and glasses relevant to geological systems, although these *in-situ* methods are useful and rapid to quantify kinetic parameters [23-24].

This contrasts with common using of such *in-situ* approaches in Glass Sciences, especially for characterizing solidification of non-crystalline solids upon heating ([25-37] and references therein). DSC is commonly used to retrieve the melting (T_m) and glass transitions (T_g) temperatures, plus key T_x (or T_c) values, i.e. the temperature of onset of crystallization. To the best of our knowledge, only [24, 38] provided crucial T_x determinations for basaltic glasses or, in general, for non-crystalline solids with chemically complex compositions as the natural ones. Most systems studied in glass sciences focus on simple compounds with only few (mainly two or three, rarely four) major components; typically, these systems solidify phases on heating or cooling, with compositions identical to those of parent glasses and liquids, respectively [23]. Instead, in natural silicate systems the number of major components are normally seven to eight and solidified phases which have stoichiometry very different from the parent liquid on cooling and/or glass during heating.

From the above literature studies is clear that there is a need to further study nucleation and growth kinetic in order to shed new light on one of the most important phenomenon linked not only to magmatic/volcanic events but also to industry. Therefore, we present new DSC investigations upon heating on six chemical complex systems. Experiments were performed by using a ramp rate of 10 °C/min from room to melting conditions. These six sub-alkaline natural compounds have chemistries ranging from SiO₂-poor basalt (B₁₀₀) to SiO₂-rich rhyolite (R₁₀₀), for which GFA is already known and determined by cooling-induced experiments via the so called *critical cooling rate* (R_c) method (for details refer to [10-11]). Experiments on re-heated and then quenched (from T_m) charges have been also structurally and chemically characterized by SEM and EPMA, to corroborate DSC data and to quantify textures and compositions of all produced phases. The

attained outcomes can be useful in scenarios where glass-bearing rocks are re-heated, i.e. flowage of lavas on volcanic rocks [16-19].

In parallel, the huge abundance of these compounds, their very cheap costs and the less effort for preparation could represent valuable alternatives to design new glass-ceramics with desired macroscopic properties for encapsulation of toxic substances.

Starting glasses, experimental and analytical methods

Starting glasses. The six different silicate starting glass compositions are the same used in [10-11]. Briefly, they were prepared by using two natural rocks: a basalt from Iceland (B₁₀₀) and rhyolite from the Lipari Island in the Aeolian arc (R₁₀₀). About 100 g of these two rocks were powdered and melted in Pt crucibles at temperature of 1600 °C for 4 h in air. After quenching on metal plates, they were crushed and re-melted two times at the same conditions in order to improve homogeneity. Then, four intermediate compositions were obtained by mechanically mixing B₁₀₀ and R₁₀₀ powders in the following proportions (by wt.%): B₈₀R₂₀, B₆₀R₄₀, B₄₀R₆₀, B₂₀R₈₀. These glassy powders were, afterwards, heat treated at identical conditions of the two end-members. The final six starting glassy compositions with systematic chemical variations, measured by EPMA (see below), are reported in Tab. 1, where are also reported the amounts of dissolved H₂O (measured by FTIR technique), densities, Fe²⁺/Fe_{tot} ratios and corresponding nomenclatures in the TAS classification diagram [10-11].

DSC (Differential Scanning Calorimetry). Single piece each ca. 125 mg of B₁₀₀, B₈₀R₂₀, B₆₀R₄₀, B₄₀R₆₀, B₂₀R₈₀ and R₁₀₀ starting glass were loaded in Al₂O₃ crucibles. The sample charges were then lodged in the DSC (Netzsch STA 449 C) and run with a heating rate of 10 °C/min, from room to melting conditions (1280 °C for of B₁₀₀ to 1130 °C for R₁₀₀), previously estimated by thermodynamic models [10]. When the liquidus region for each system was achieved, the sample-charges were rapidly quenched to ambient conditions. A duplicate DSC experiment was run for B₁₀₀ using the same thermal program, but instead a Pt-crucible was used in order to evaluate the possible effect that sample holder could have on phase nucleation and growth. The same apparatus was also used to bracket *in-situ* the *R_c* (GFA) of B₁₀₀ [10, 11] following the method of [38].

SEM and EPMA analyses. The quenched run products were mounted in epoxy and polished for textural and chemical analysis. Images of phases and their textures were first identified and collected by back-scattered electrons using a field-emission JEOL 6500 F scanning electron microscopy, equipped with an energy-dispersive spectrometer (EDS). Their chemical attributes were then accurately determined with a JEOL JXA 8200 electron probe micro-analyzer equipped with five wavelength-dispersive spectrometers (WDS). Both these facilities are installed at the HP-

HT laboratory of Volcanology and Geophysics of Istituto Nazionale di Geofisica e Vulcanologia (Rome, Italy). The operative conditions and data reduction obtained by FE-SEM and EPMA are extensively reported in [39-41] and [10-11].

In particular, the chemical characterization of phases with a diameter > 1 and < 3 μm was obtained by the EDS of SEM, whereas those ≥ 3 μm by EPMA. The differences of average chemical compositions measured either by EPMA and FE-SEM were negligible, as indicated by analyses on the same glass matrix portions as reported in [11]. The textures of run-products, i.e. type, size and distribution of each phase, have been first evaluated on back-scattered SEM microphotographs collected at 150, 400, 800 and 1500 X magnifications. As a function of these first qualitative observations, image analysis has been performed following classical procedures reported in details by [3, 39-43]. Such analyses have been achieved on BSE images that better represent the whole texture in all the run-products. Quantitative textures of crystal-bearing B₁₀₀, B₈₀R₂₀ and B₆₀R₄₀ run-products were considered in two ways, i.e. in contact and beyond a distance of 100 μm from the Al₂O₃ sample holder wall in order to evaluate possible effects of Al₂O₃ on nucleation [10, 44].

Results

DSC. The six DSC spectra for B₁₀₀, B₈₀R₂₀, B₆₀R₄₀, B₄₀R₆₀, B₂₀R₈₀ and R₁₀₀ collected from experiments performed in Al₂O₃ crucibles and those recorded in Pt for B₁₀₀, are stacked in Fig. 1. R₁₀₀ and B₂₀R₈₀ DSC spectra do not show any evident peaks. *T_g* and *T_m* peaks for B₁₀₀, B₈₀R₂₀, B₆₀R₄₀ and B₄₀R₆₀ have respectively very low to high endothermic intensities, whereas *T_x* is marked by high exothermic peaks. *T_g*, *T_x* and *T_m* are progressive less noticeable when moving from SiO₂-poor (B₁₀₀) to SiO₂-rich (B₄₀R₆₀) systems (Fig. 1). The DSC thermograms of B₁₀₀ run with Al₂O₃ and Pt sample holders show identical *T_g*, *T_x* and *T_m* peak positions, but the ratio between signal and background is higher for spectrum collected with the Pt charge than the Al₂O₃; furthermore, only the DSC spectra of B₁₀₀ show a low intense exothermic peak between *T_x* and *T_m*, indicative of a secondary crystallization event (Fig. 1).

The values of *T_g*, *T_x* and *T_m* are reported in Tab. 2. In Tab. 1 are also reported the modelled values of **T_m* and **T_g*, showing differences with *T_m* and *T_g* measured by DSC respectively of 29 and 41 °C for B₁₀₀, 9 and 29 °C for B₈₀R₂₀, 20 and 27 °C for B₆₀R₄₀ and of 9 and 18 °C for B₄₀R₆₀. Hence, the DSC kinetic determinations of *T_g* and *T_m* agree with those calculated at equilibrium conditions with available thermodynamic and rheological models, being differences lesser than 30 and 42 °C, respectively. The trend of *T_g*, *T_x* and *T_m* as a function of SiO₂ of the bulk system are

diagrammed in Fig. 2. T_g changes of only 10 °C (Tab. 2), T_m first decreases and then levels off and T_x show evident higher linear increasing moving from B₁₀₀ to B₄₀R₆₀ (Fig. 2).

The GFA character of B₁₀₀ has been measured *in-situ* here, following the approach described in [24, 38] of heating and cooling cycles. The related thermograms and derived peaks areas, as a function of cooling rate, are displayed in Fig. 3. The area of peaks moderately increases for rates between 5 and 10 and then rapidly augments from 10 to 45 K/min; however, the plateau value indicative of the R_c has been un-attained. Hence, DSC data indicate that the R_c value for B₁₀₀ is higher than 45 °C/min or 4050 °C/h in agreement with the R_c of about 9000 °C/h determined by serial cooling rate *ex-situ* experiments by [10-11].

Textures of phases. The general and salient textural features of the B₁₀₀, B₈₀R₂₀, B₆₀R₄₀ and B₄₀R₆₀ crystal-bearing run-products are displayed at variable magnifications in Fig. 4. Qualitatively, the increasing of SiO₂ in the bulk system (B₁₀₀ to B₄₀R₆₀) induces a reduction of the amount and size of crystalline phases. Sp is ubiquitous in any of the run-products with size of several μm in B₁₀₀, around 1 μm in B₈₀R₂₀ and sub-micrometric for both B₆₀R₄₀ and B₄₀R₆₀. Cpx occurs in B₁₀₀, B₈₀R₂₀ and B₆₀R₄₀ with size of few tens of μm in B₁₀₀ with irregular to dendritic shapes, lengths lower than 10 μm in B₈₀R₂₀ mainly with dendritic aspect and like tiny elongated dendrites of only few μm in B₆₀R₄₀ system (Fig. 4). Cpx crystals branches out preferentially from single sp crystals; textures of both sp and cpx appears distributing along strips in B₁₀₀, more randomly and homogeneously spread in B₈₀R₂₀, whereas in B₆₀R₄₀ cpx and sp are agglomerated in relative crystal-rich patches in an intra-crystalline dark glass, surrounded by a glass matrix (Fig. 4). On the other hand, plg is present only on the rim of Al₂O₃ sample holder, showing prismatic to acicular crystal shape with the longest size nearly perpendicular to capsule walls (Fig. 4). Plg is relatively abundant in B₁₀₀, moderate for B₈₀R₂₀, very low for B₆₀R₄₀ and undetectable for the B₄₀R₆₀ system; plg disappears at a linear distance from the Al₂O₃ wall of some tens of μm in B₁₀₀ and even at shorter distance (closer to the sample holder) for the other two B₈₀R₂₀ and B₆₀R₄₀ compositions (Fig. 4).

The area% of plg, cpx, sp and glass phases are reported in Tab. 3, either far or close from alumina surfaces; the former situation is unaffected by Al₂O₃ and thus is representing the actual and intrinsic crystallization behaviour of these whole glass systems. The evolution of phases contents as a function of bulk SiO₂ is shown in Fig. 5. The amount of sp is < 4 area% and follows a moderate concave upward trend with maxima at B₁₀₀ and B₄₀R₆₀ system. Cpx area% decrease from about 50 to 40 between B₁₀₀ and B₈₀R₂₀, down to 16 area % in B₆₀R₄₀. The glass phases, either matrix or intra-crystalline, rapidly and almost linear increasing from B₁₀₀ to B₄₀R₆₀ and it represents the unique phase in B₂₀R₈₀ and R₁₀₀ (Fig. 5).

Compositions of phases. The majority of crystalline phases have very tiny size dimensions; in turn, only cpx crystals in B₁₀₀ can be quantifiable by EPMA (Tab. 4). The chemical features of the major oxide amounts in the starting glass systems and those measured after quenching are compared in Fig. 6. Oxides in B₆₀R₄₀, B₄₀R₆₀, B₂₀R₈₀ and R₁₀₀ quenched glasses have almost identical compositions of their bulk chemistries, whereas both B₁₀₀ and B₈₀R₂₀ are enriched in SiO₂, Al₂O₃ and Na₂O and poorer in TiO₂ (only for B₁₀₀), Fe₂O₃, MgO and CaO, respectively (Fig. 6). The correspondence of all chemical oxides of B₆₀R₄₀, B₄₀R₆₀, B₂₀R₈₀ and R₁₀₀ on 1:1 line corroborate the very low amount and absence of crystalline phases measured by textures (Tab. 3 and Fig. 5), whereas those quantified in B₁₀₀ and B₈₀R₂₀ are mainly due to the solidification of cpx (Tab. 4 and Fig. 6). The average crystal-chemical formula of it in B₁₀₀, according to EPMA data (Tab. 4) and crystal-chemical constrains of single-chain clinopyroxenes [45-46] is $M^{2}(Na_{0.03}Ca_{0.68}Fe^{2+}_{0.18}Mg_{0.11})^{M1}(Mg_{0.67}Fe^{3+}_{0.09}Al_{0.21}Ti_{0.03})^{T}(Al_{0.32}Si_{1.68})O_6$; the marked peculiarity of this cation ordering is the presence of significant amount of Al, either in T- and M1-sites, similarly to cpx grown under kinetics conditions in an alkali basalt by [47].

Discussion

The GS attributes of all the six bulk chemical systems investigated by *in-situ* DSC (Tabs. 1 and 2, Figs. 1 and 2) corroborate well by *ex-situ* textural and micro-chemical outcomes (Tabs. 3 and 4, Figs. 3, 4 and 5). The heating rate of 10 °C/min or 600 °C/h is too high to permit crystal nucleation in R₁₀₀ and B₂₀R₈₀. It is close to a critical heating rate for B₄₀R₆₀ and becomes progressively more amenable to crystal nucleation for B₆₀R₄₀, B₈₀R₂₀ and B₁₀₀ systems, according to their amounts of crystals (Tabs. 2 and 3, Figs. 1, 2, 3 and 4). Thus, B₆₀R₄₀, B₈₀R₂₀ and B₁₀₀ chemical systems require progressive higher rates to avoid nucleation upon heating, whereas R₁₀₀ and B₂₀R₈₀ necessitate lower heating rates to initiate nucleation. Therefore, the amount of SiO₂ or the NBO/T parameter scale with a critical heating rate and GS, similarly to those demonstrated experimentally with GFA *via Rc* [11].

The thermal range between T_m and T_g for B₁₀₀, B₈₀R₂₀, B₆₀R₄₀ and B₄₀R₆₀ is 512, 501, 462 and 460 °C, respectively (Tab. 2). Since the heating rate is 10 °C/min, these glasses were re-heated dynamically for 50/45 minutes between T_g and T_m , allowing crystallization of 51.5, 41.5, 17.4 and only 3 area% (Tab. 2) of crystals for B₁₀₀, B₈₀R₂₀, B₆₀R₄₀ and B₄₀R₆₀, respectively. These results globally corroborate with those obtained by isothermal (fixed T , variable t) re-heating experiments and related TTT diagrams performed on basaltic to basaltic-andesites glasses by [20-22]. These previous studies highlight that re-crystallization is extensive and requires even few minutes at

intermediate T , whereas is moderate to weak and necessitates tens of minutes when isothermal treatment is close to T_m or T_g .

These GS behaviours of chemically-complex sub-alkaline systems can be validated here quantitatively and can be compared and relates with GFA. GS has been computed in different ways, using the most known and used parameters:

$$K_T = T_g / T_m \text{ [48]}$$

$$K_H = (T_x - T_g) / (T_m - T_x) \text{ [22]}$$

$$K_W = (T_x - T_g) / T_m \text{ [23]}$$

$$K_{LL} = T_x / (T_g + T_m) \text{ [26]}$$

$$w_2 = (T_g / T_m) - (T_g / (2T_x - T_g)) \text{ [49]}.$$

which combine T_m , T_g and T_x , (Tab. 2). According to DSC data and critical heating rate (see above), in Fig. 7 are displayed all the GS parameters as a function of SiO_2 , i.e. those of $\text{B}_{40}\text{R}_{60}$, $\text{B}_{60}\text{R}_{40}$, $\text{B}_{80}\text{R}_{20}$ and B_{100} systems. Each GS parameter increases when SiO_2 augments, along linear trends. The linear regressions show relatively low R^2 for K_T , the so-called reduced glass transition, which does not include T_x , whereas all the others including T_x have very high R^2 values (Tab. 2 and Fig. 7). The same relationships and regressions are provided when GS parameters are plotted *versus* NBO/T (Tab. 1). Therefore, T_x and GS are both linearly proportional to sub-alkaline chemical composition, either SiO_2 or NBO/T (Figs. 2 and 7); in other words, enrichment of SiO_2 or decreasing of NBO/T in sub-alkaline glasses enhance their stability upon heating or, alternatively, progressively impede their nucleation.

The GS attributes are frequently used to retrieve the GFA [26-37, 48-49]. Therefore, it is possible to relate GS parameters (by considering those glass as the most widespread compositions on Earth), by comparing R_c with GS parameters as well as with T_x . These comparisons are displayed in Fig. 8, showing that the increasing of R_c as a function of bulk chemical systems for B_{100} , $\text{B}_{80}\text{R}_{20}$, $\text{B}_{60}\text{R}_{40}$, and $\text{B}_{40}\text{R}_{60}$ (determined in [11]), is inversely and linearly correlated with T_x and K_W , K_{LL} and w_2 , with high correlations degree (Fig. 8).

These relationships prove that natural sub-alkaline glasses, characterised by a large amount of chemical elements (O, Si, Ti, Al, Fe, Mg, Ca, Na and K), remain more easily in glassy state when heated from ambient to *liquidus* conditions and more easily will form a glass when cooled from *liquidus* to room conditions as a function of increasing SiO_2 or decreasing of NBO/T. The straightforward corollary is that the decreasing of SiO_2 , or increasing of NBO/T, progressively facilitates nucleation. Under natural conditions, SiO_2 -rich glasses hosted in volcanic rocks have high chance to persist to thermal perturbations, whereas SiO_2 -poor ones can be transformed relatively fast and easily, being prone to nucleate. The same general behaviour holds under cooling

from completely molten bulk silicate systems. The GS and GFA characteristics highlighted here, as a function of compositions and thermal treatments, can be used to design glasses and glass-ceramics with the lowest costs of raw-materials and by far the most abundant on Earth.

Acknowledgments

This work was funded by the “fondi ateneo” of the University G. d’Annunzio of Chieti-Pescara assigned to Iezzi G.. Vetere F. acknowledges the European Research Council for the Consolidator Grant ERC-2013-CoG Proposal No. 612776 — CHRONOS to Perugini D. and support from the TESLA FRB-base project from the Department of Physics and Geology, University of Perugia.

References

- [1] K.V. Cashman, Relationship between plagioclase crystallization and cooling rate in basaltic melts *Contributions to Mineralogy and Petrology* 113 (1989) 126-142.
- [2] A.C. Lasaga, *Kinetic Theory in the Earth Sciences*. Princeton University Press, Princeton, New York (1997).
- [3] M.D. Higgins, *Quantitative Textural Measurements in Igneous and Metamorphic Petrology*. Cambridge University Press, Cambridge (2006).
- [4] J.E. Hammer, Experimental studies of the kinetics and energetics of magma crystallization, in: Putirka, K.D., Tepley, F.J. (Eds.). *Reviews in Mineralogy* 69 (2008) 9-59.
- [5] G. Iezzi, S. Mollo, G. Ventura, A. Cavallo, C. Romano, Experimental solidification of anhydrous latitic and trachytic melts at different cooling rates: the role of nucleation kinetics. *Chemical Geology* 253 (2008) 91-101.
- [6] G. Iezzi, S. Mollo, G. Ventura, Solidification behaviour of natural silicate melts and volcanological implications, in: Lewis, N., Moretti, A. (Eds.), *Volcanoes: Formation, Eruptions and Modelling*. Nova publishers, New York (2009) 127-151.
- [7] G. Iezzi, S. Mollo, Torresi, G. Ventura, A. Cavallo, P. Scarlato, Experimental solidification of an andesitic melt by cooling. *Chemical Geology* 283 (2011) 261-273.
- [8] P. Del Gaudio, S. Mollo, G. Ventura, G. Iezzi, J. Taddeucci, A. Cavallo, Cooling rate-induced differentiation in anhydrous and hydrous basalts at 500 MPa: implications for the storage and transport of magmas in dikes. *Chemical Geology* 270 (2010) 164-178.
- [9] S. Mollo, G. Iezzi, G. Ventura, A. Cavallo, P. Scarlato, Heterogeneous nucleation mechanisms and formation of metastable phase assemblages induced by different crystalline seeds *Journal of Non-Crystalline Solids* 358 (2012) 1624-1628.
- [10] F. Vetere, G. Iezzi, H. Behrens, A. Cavallo, V. Misiti, M. Dietrich, J. Knipping, G. Ventura, S. Mollo, Intrinsic solidification behaviour of basaltic to rhyolitic melts: a cooling rate experimental study. *Chemical Geology* 354 (2013) 233-242.
- [11] F. Vetere, G. Iezzi, H. Behrens, F. Holtz, G. Ventura, V. Misiti, A. Cavallo, S. Mollo, M. Dietrich, Glass forming ability and crystallization behaviour of sub-alkaline silicate melts. *Earth-Science Reviews* 150 (2015) 25-44.
- [12] P. Armienti, Decryption of igneous rock textures: crystal size distribution tools, in: Putirka, K.D., Tepley, F.J. (Eds.). *Reviews in Mineralogy* 69 (2008) 623-649.
- [13] L.J. Applergarth, H., Tuffen M.R. James, H. Pinkerton, *Earth-Science Reviews* 116 (2013) 1-16.

[14] Arzilli, F., Carroll, M.R. (2013). Crystallization kinetics of alkali feldspars in cooling and decompression-induced crystallization experiments in trachytic melt. *Contributions to Mineralogy and Petrology* 166 1011-1027.

[15] A. Fiege, F. Vetere, G. Iezzi, A. Simon, F. Holtz, The roles of decompression rate and volatiles ($H_2O+Cl\pm CO_2\pm S$) on crystallization in (trachy-) basaltic magma. *Chemical Geology* 411 (2015) 310-322.

[16] D.J.M. Burkhard, Crystallization and oxidation during emplacement of lava lobes. *Special Paper of the Geological Society of America* 396 (2005a) 67-80.

[17] D.J.M. Burkhard, Nucleation and growth rates of pyroxene, plagioclase, and Fe-Ti oxides in basalt under atmospheric conditions. *European Journal of Mineralogy* 17 (2005b) 675-685.

[18] D.J.M. Burkhard, Thermal interaction between lava lobes. *Bulletin of Volcanology* 65 (2-3) (2003) 136-143.

[19] D.J.M. Burkhard, Crystallization and oxidation of Kilauea basalt glass: Processes during reheating experiments. *Journal of Petrology* 42 (3) (2001) 507-527.

[20] N. Dearn, K. Cashman, Rapid crystallization during recycling of basaltic andesite tephra: timescales determined by reheating experiments. *Scientific Reports* 7 (2017) 46364

[21]. D'Oriano, C., M. Pompilio, A. Bertagnini, R. Cioni, M. Pichavant, Effects of experimental reheating of natural basaltic ash at different temperatures and redox conditions. *Contrib Mineral Petr* 165 (2013) 863–883 doi: 10.1007/s00410-012-0839-0.

[22]. C. D'Oriano, A. Bertagnini, R. Cioni, M. Pompilio, Identifying recycled ash in basaltic eruptions. *Sci Rep-Uk* 4, (2014) doi: ARTN 585110.1038/srep05851.

[23] J.E. Shelby, *Introduction to Glass Science and Technology*, 2nd edition. Padstow, Cornwall, UK (2005).

[24] C.S. Ray, S.T. Reis, S. Sen, J.S. O'Dell, JSC-1A lunar soil simulant: Characterization, glass formation, and selected glass properties. *Journal of Non-Crystalline Solids* 356 (2010) 2369-2374.

[25] A. Hrubý, Evaluation of glass-forming tendency by means of DTA. *Czechoslovak Journal of Physics B* 22 (1972) 1187–1193.

[26] M.C. Weinberg, Glass-forming ability and glass stability in simple systems. *Journal of Non-Crystalline Solids* 167 (1994) 81-88.

[27] A.A. Cabral, C. Fredericci, E.D. Zanotto, A test of the Hrubý parameter to estimate glass-forming ability. *Journal of Non-Crystalline Solids* 219 (1997) 182-186.

[28] A.A. Cabral, A.A.D. Cardoso, E.D. Zanotto, Glass-forming ability versus stability of silicate glasses. I. Experimental test. *Journal of Non-Crystalline Solids* 320 (2003) 1-8

[29] Z.P. Lu, C.T. Liu, A new glass-forming ability criterion for bulk metallic glasses. *Acta Mater.* 50 (2002) 3501-3512.

[30] Long, Z., Wei, H., Ding, Y., (...), Xie, G., Inoue, A. (2009). A new criterion for predicting the glass-forming ability of bulk metallic glasses. *Journal of Alloys and Compounds*, 475(1-2), pp. 207-219.

[31] Zhang, P., Wei, H., Wei, X., Long, Z., Su, X. (2009). Evaluation of glass-forming ability for bulk metallic glasses based on characteristic temperatures. *Journal of Non-Crystalline Solids*, 355, 2183-2189.

[32] Nascimento, M.L.F., Souza, L.A., Ferreira, E.B., Zanotto, E.D. (2005). Can glass stability parameters infer glass forming ability?. *Journal of Non-Crystalline Solids*, 351(40-42), pp. 3296-3308.

[33] A.F. Kozmidis-Petrović, Sensitivity of the Hrubby, Lu-Liu, Fan, Yuan, and Long glass stability parameters to the change of the ratios of characteristic temperatures T_x/T_g and T_m/T_g . *Thermochimica Acta* 510 (2010a) 137-143.

[34] A.F. Kozmidis-Petrović, Theoretical analysis of relative changes of the Hrubby, Weinberg, and Lu-Liu glass stability parameters with application on some oxide and chalcogenide glasses. *Thermochimica Acta* 510 (2010b) 54-60

[35] A.F. Kozmidis-Petrović, Which glass stability criterion is the best? *Thermochimica Acta* 523 (2011) 116-123

[36] E. B. Ferreira, E. D. Zanotto, S. Feller, G. Lodden, J. Banerjee, T. Edwards, M. Affatigato, Critical Analysis of Glass Stability Parameters and Application to Lithium Borate Glasses 94 (2011) 3833-3841

[37] T.V.R. Marques, A.A. Cabral, Influence of the heating rates on the correlation between glass-forming ability (GFA) and glass stability (GS) parameters. *Journal of Non-Crystalline Solids* 390 (2014) 70-76.

[38] C.S. Ray, S.T. Reis, R.K. Brow, W. Höland, V. Rheinberger, A new DTA method for measuring critical cooling rate for glass formation. *Journal of Non-Crystalline Solids* 351 (2005) 1350-1358.

[39] G. Iezzi, S. Mollo, G. Ventura, A. Cavallo, C. Romano, Experimental solidification of anhydrous latitic and trachytic melts at different cooling rates: the role of nucleation kinetics. *Chem. Geol.* 253 (2008) 91–101.

- [40] G. Iezzi, S. Mollo, G. Torresi, G. Ventura, A. Cavallo, P. Scarlato, Experimental solidification of an andesitic melt by cooling. *Chem. Geol.* 283 (2011) 261–273.
- [41] G. Iezzi, S. Mollo, E. Shahini, A. Cavallo, P. Scarlato, The cooling kinetics of plagioclase feldspars as revealed by electron-microprobe mapping. *American Mineralogist* 99 (2014a) 898–907.
- [42] G. Iezzi, C. Caso, G. Ventura, M. Vallefucio, A. Cavallo, H. Behrens, S. Mollo, D. Paltrinieri, P. Signanini, F. Vetere, Historical volcanism at the Marsili Seamount (Tyrrhenian Sea, Italy): first documented deep submarine explosive eruptions in the Mediterranean Sea. *Gondwana research* 25 (2014b) 764-774.
- [43] G. Lanzafame, S. Mollo, G. Iezzi, C. Ferlito, G. Ventura, Unraveling the solidification path of a pahoehoe “cicirara” lava from Mount Etna volcano. *Bulletin of Volcanology* 75 (2013) 1-16.
- [44] S. Mollo, G. Iezzi, G. Ventura, A. Cavallo, P. Scarlato Heterogeneous nucleation mechanisms and formation of metastable phase assemblages induced by different crystalline seeds in a rapidly cooled andesitic melt. *Journal of Non-Crystalline Solids* 358 (2012)1624-1628.
- [45] W.A Deer, R.A. Howie, and J. Zussman, Rock forming minerals, Doublechain Silicates. Longman Scientific and Technical (1997).
- [46] G. Iezzi, G. D. Bromiley, A. Cavallo, P. P. Das, F. Karavassili, I. Margiolaki, A. A. Stewart, M. Tribaudino, J. P. Wright, Solid solution along the synthetic $\text{LiAlSi}_2\text{O}_6$ - $\text{LiFeSi}_2\text{O}_6$ (spodumene-ferri-spodumene) join: A general picture of solid solutions, bond lengths, lattice strains, steric effects, symmetries, and chemical compositions of Li clinopyroxenes, *American Mineralogist* 101 (2016) 2498-2513.
- [47] S. Mollo, P. Del Gaudio, G. Ventura, G. Iezzi, P. Scarlato, Dependence of clinopyroxene composition on cooling rate in basaltic magmas: implications for thermobarometry. *Lithos*, 118 (2010) 302-312.
- [48] D. Turnbull, Under what conditions can a glass be formed? *Contemporary Physics* 10 (1969) 473-488.
- [49] B. Gu, F. Liu, Y. Jiang, K. Zhang, Evaluation of glass-forming ability criterion from phase-transformation kinetics. *Journal of Non-Crystalline Solids* 358 (2012) 1764-1771.
- [50] G.H. Klöß, Dichtefluktuationen natürlicher Gläser (Dissertation) University of Jena (2000).
- [51] H. Hui, Y. Zhang, Toward a general viscosity equation for natural anhydrous and hydrous silicate melts. *Geochim. Cosmochim. Acta* 71 (2007) 403–416.

Table captions

Table 1. Chemical compositions of the six glass starting materials.

Footnotes: averages and standard deviations of major components are in wt. %, obtained on at least 15 EPMA point analyses; Fe^{2+}/Fe_{tot} was determined for each sample using a modified Wilson method as described in [10]. H_2O content was measured by IR spectroscopy using the peak height of the absorption band at 3550 cm^{-1} [10]. Glass density was estimated using the model of [50] already reported in [10]. T_m and T_g ($^{\circ}C$ at 10^{12} Pa s) are calculated using MELTS (Ghiorso and Sacks, 1994) and the general viscosity model from [51], respectively. T_{rg} is T_g/T_m .

Table 2. T_g , T_x and T_m determined by DSC at a heating rate of $10\text{ }^{\circ}C/\text{min}$ up to $1300\text{ }^{\circ}C$ from DSC spectra of Fig. 1. The calculated glass stability parameters are also reported.

Footnotes: $K_T = T_g / T_m$ [48]; $K_H = (T_x - T_g) / (T_m - T_x)$ [22]; $K_W = (T_x - T_g) / T_m$ [23]; $K_{LL} = T_x / (T_g + T_m)$ [26]; $w_2 = (T_g / T_m) - (T_g / (2T_x - T_g))$ [49].

Table 3. Textural features of run-products quenched after the heating rate of $10\text{ }^{\circ}C/\text{min}$ up to $1300\text{ }^{\circ}C$.

Footnotes: * the crystal texture distributions are invariably homogeneous following the criteria proposed by Vetere et al . (2013 and 2014). B_{100} magnifications used 150, 400, 800 and 1500 X; $B_{80}R_{20}$ magnifications used 400, 800 and 1500 X; $B_{60}R_{40}$ magnifications used 800 and 1500 X; $B_{40}R_{60}$ magnifications used 800, 1500 and 4000 X.

Table 4. Average and standard deviation chemical compositions of phases in run-products quenched after the heating rate of $10\text{ }^{\circ}C/\text{min}$ up to $1300\text{ }^{\circ}C$.

Figure Captions

Figure 1. DSC spectra of the six glasses heated at 10 °C/min. All glasses were measured using alumina holders, except the B₁₀₀ measured either in Pt (dashed red line) and alumina sample holders. The glass transition, onset of crystallization and melting temperatures (T_g , T_x and T_m , respectively) are indicated by arrows. The B₂₀-R₈₀ and R₁₀₀ compositions do not show any peak. From B₁₀₀ down to B₄₀R₆₀ the peaks are progressively less prominent.

Figure 2. Evolution of T_g , T_x and T_m as a function of SiO₂ (wt.%). T_g is nearly constant, whereas T_x and T_m increase and decrease, respectively from B₁₀₀ to B₄₀R₆₀.

Figure 3. (left) Glass forming ability of B₁₀₀ determined by DSC spectra at various heating and cooling rates following the method of Ray et al. (2005) and (right) related DSC peak area vs cooling rate, showing the absence of a plateau indicative that the critical cooling rate (R_c) of B₁₀₀ is > 45 °C/min.

Figure 4. Phase assemblages by FE-SEM images of run-products heated at 10 °C/min in alumina sample-holders. From B₁₀₀ (top row) to B₄₀R₆₀ (last row) the amount of glass (gl) increases, whereas that of pyroxene (px) decreases; the amount of spinel (sp) is invariably few area%. Plagioclase crystallizes heterogeneously only on the alumina sample holders in B₁₀₀ and B₈₀R₂₀.

Figure 5. Phase amounts as a function of SiO₂ (wt.%) of the bulk system. From B₁₀₀ to B₄₀R₆₀ the amount of glass (gl) increases, that of pyroxene (px) decreases (B₁₀₀ to B₆₀R₄₀) and then disappears (B₄₀R₆₀), whereas the amount of spinel (sp) is invariably few area%.

Figure 6. Starting chemical compositions vs their corresponding glass (residual melt) and cpx (only B₁₀₀ cpx crystals were measurable) compositions. R₁₀₀, B₂₀R₈₀, B₄₀R₆₀ and B₆₀R₄₀ glasses have oxides equal to their starting compositions (except slight differences for Al₂O₃ amounts) in agreement with the absence (R₁₀₀, B₂₀R₈₀ and B₄₀R₆₀) or very slight crystallisation during heating. B₁₀₀ and B₈₀R₂₀ have residual melts enriched in SiO₂, Al₂O₃ and Na₂O and depauperated in Fe₂O₃, MgO and CaO compared to their starting oxide corresponding amounts due to a significant crystallisation of sp (spinel) and especially cpx, in agreement with the textural data reported in Table 3 and Figs. 3 and 4. The cpx in B₁₀₀ is relatively rich in CaO and MgO.

Figure 7. Principal glass stability parameters (see Table 2 for labels and calculations). All parameters increase linearly and monotonically as a function of SiO₂ or NBO/T (see Table 1). The dotted lines are guide for eye, whereas the linear regressions R² index shown in the legend refer to linear regressions of SiO₂ vs glass stability parameters.

Figure 8. Relations among the critical cooling rates (R_c) and their corresponding glass stability parameters (see Table 2 for labels and calculations) for B₁₀₀, B₈₀R₂₀, B₆₀R₄₀ and B₄₀R₆₀ bulk systems, respectively (bottom diagram); relation between the critical cooling rates (R_c) and T_x for B₁₀₀, B₈₀R₂₀, B₆₀R₄₀ and B₄₀R₆₀, respectively (top diagram). Lines are linear regressions with R² index reported in the legend. The critical cooling rates (R_c) are measured in Vetere et al. (2015). These plots highlights that glass stability and glass forming ability features are strongly related for natural sub-alkaline silicate melts, i.e. a melt and its corresponding glass are both reluctant to nucleate on cooling and heating, respectively.

Table 3

system	SiO ₂	phase contents > 100 µm from Al walls					phase contents ≤ 100 µm from Al walls				
		glass	cpx	sp	# BSE images	*phase distribution	glass	plg	cpx	sp	# BSE images
B ₁₀₀	48.02	48.5 (1.8)	47.7 (1.7)	3.8 (1.2)	4	H	29.4 (21.9)	11.6 (9.5)	54.3 (12.5)	4.8 (0.1)	2
B ₈₀ R ₂₀	53.01	58.5 (2.4)	40.6 (2.4)	0.9 (0.2)	4	H	52.9 (10.9)	8.0 (10.0)	38.1 (0.9)	1.1 (0.1)	2
B ₆₀ R ₄₀	57.97	82.6 (4.9)	16.0 (3.8)	1.3 (1.2)	6	H	68.9	1.3	25.3	4.5	1
B ₄₀ R ₆₀	62.73	97.0 (1.0)	-	3.0 (1.0)	5	H	-	-	-	-	-
B ₂₀ R ₈₀	67.91	-	-	-	-	-	-	-	-	-	-
R ₁₀₀	73.97	-	-	-	-	-	-	-	-	-	-

Table 4

system	phase	# point analysed	SiO ₂	TiO ₂	Al ₂ O ₃	Fe ₂ O ₃	MnO	MgO	CaO	Na ₂ O	K ₂ O	total
B ₁₀₀	glass	12	54.33 (0.55)	0.84 (0.16)	19.78 (1.41)	8.20 (0.83)	0.14 (0.10)	4.41 (0.89)	9.99 (0.51)	2.78 (0.28)	0.06 (0.03)	100.53 (0.52)
	cpx	9	45.66 (0.87)	1.16 (0.02)	12.30 (1.12)	9.91 (0.61)	0.01 (0.01)	14.08 (0.81)	17.37 (1.51)	0.47 (0.26)	0.03 (0.02)	100.92 (0.77)
B ₈₀ R ₂₀	glass	11	56.56 (0.75)	0.86 (0.08)	18.34 (0.41)	7.79 (0.46)	0.11 (0.08)	3.93 (0.58)	8.70 (0.54)	3.02 (0.21)	1.21 (0.09)	100.51 (0.38)
B ₆₀ R ₄₀	glass	12	58.38 (0.53)	0.60 (0.15)	15.41 (0.22)	7.91 (0.39)	0.13 (0.08)	5.75 (0.18)	8.64 (0.21)	2.38 (0.15)	1.60 (0.10)	100.09 (0.64)
B ₄₀ R ₆₀	glass	9	63.63 (0.34)	0.44 (0.08)	14.92 (0.15)	5.62 (0.26)	0.12 (0.06)	4.19 (0.12)	5.94 (0.15)	3.00 (0.11)	2.92 (0.06)	100.23 (0.31)
B ₂₀ R ₈₀	glass	8	68.09 (0.58)	0.30 (0.10)	14.39 (0.57)	4.00 (0.27)	0.12 (0.05)	2.38 (0.17)	3.75 (0.09)	3.37 (0.16)	3.88 (0.08)	100.28 (0.61)
R ₁₀₀	glass	8	73.24 (0.37)	0.13 (0.05)	13.32 (0.23)	2.25 (0.11)	0.09 (0.05)	0.50 (0.08)	1.30 (0.06)	3.53 (0.09)	4.84 (0.13)	99.20 (0.33)

Figure 1

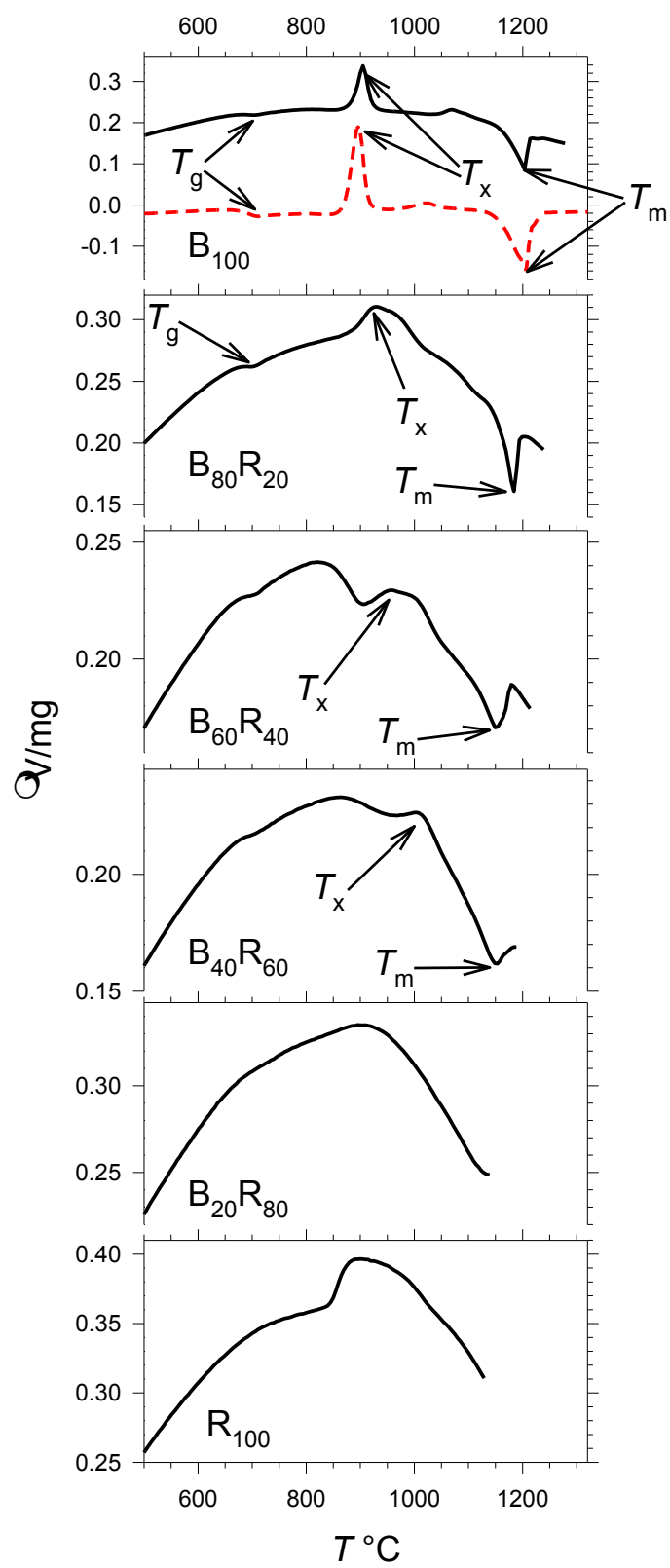


Figure 2

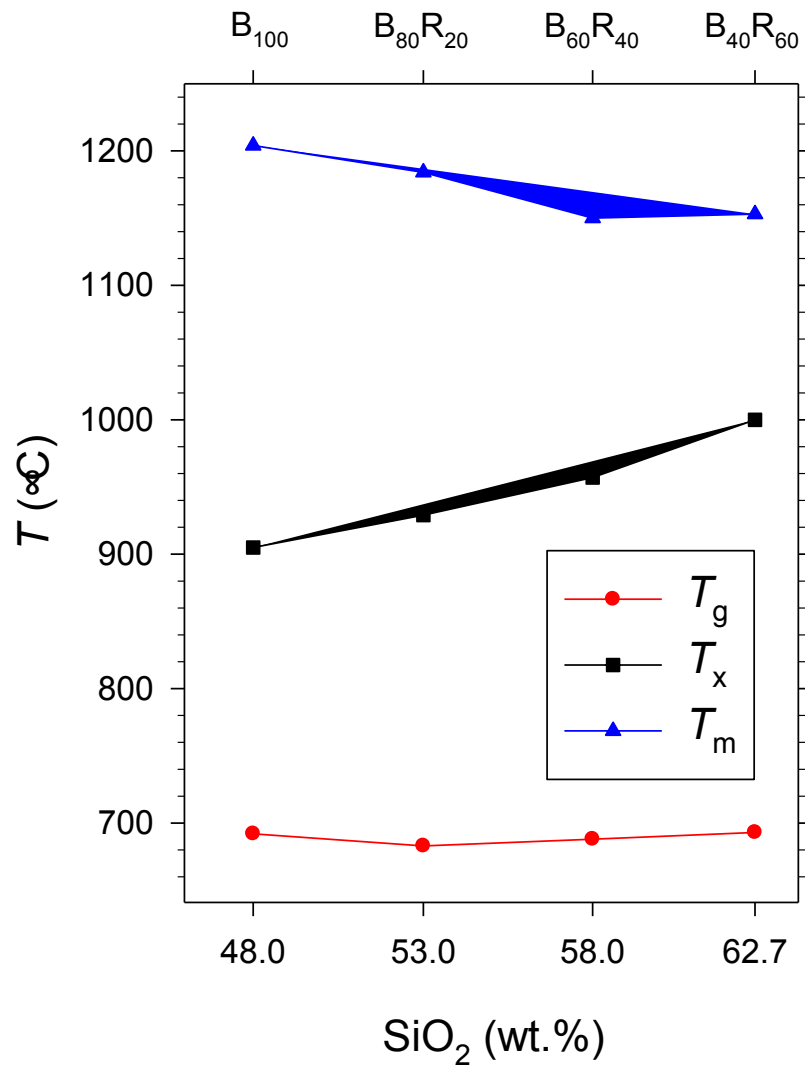


Figure 3

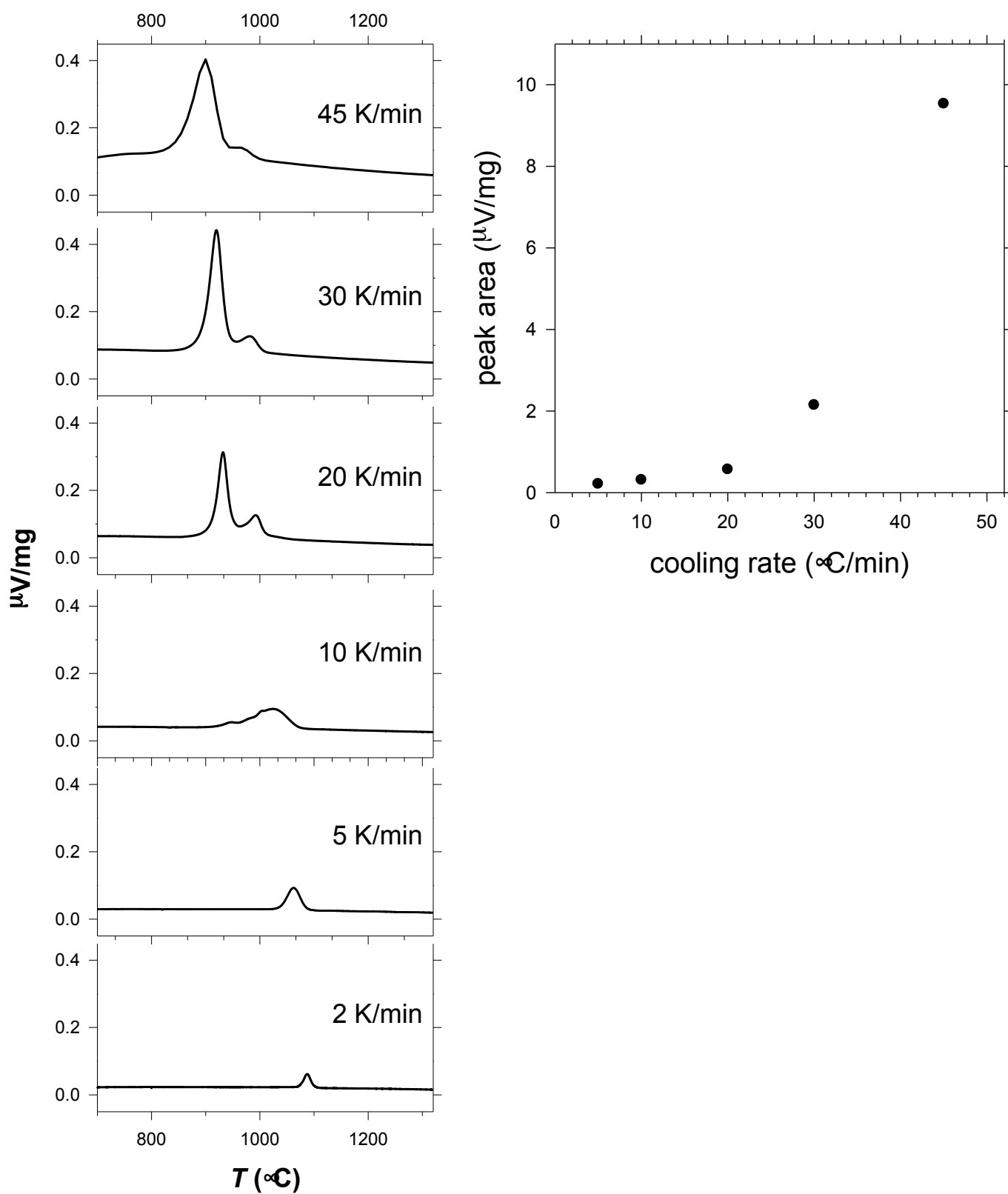


Figure 4

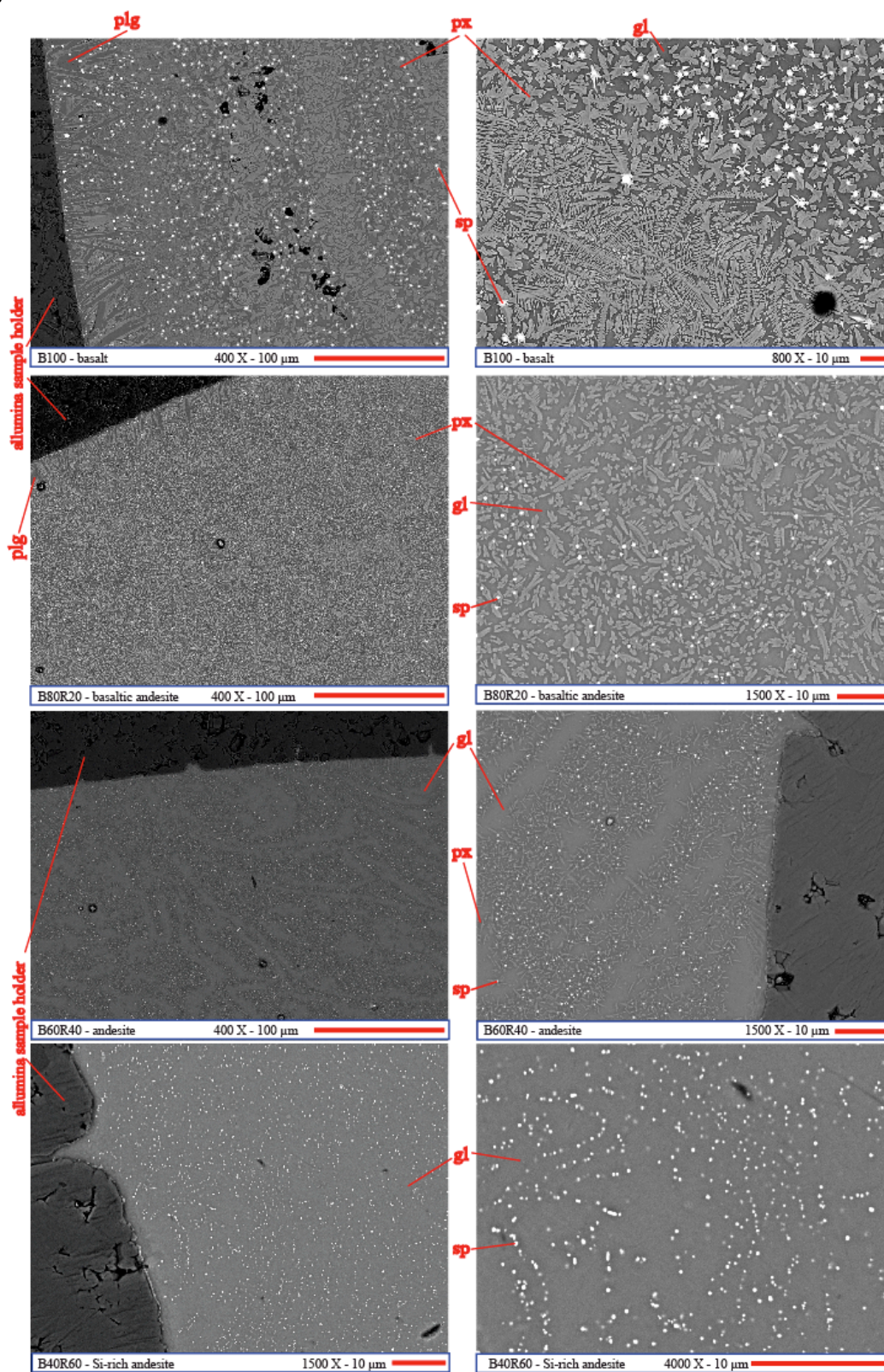


Figure 5

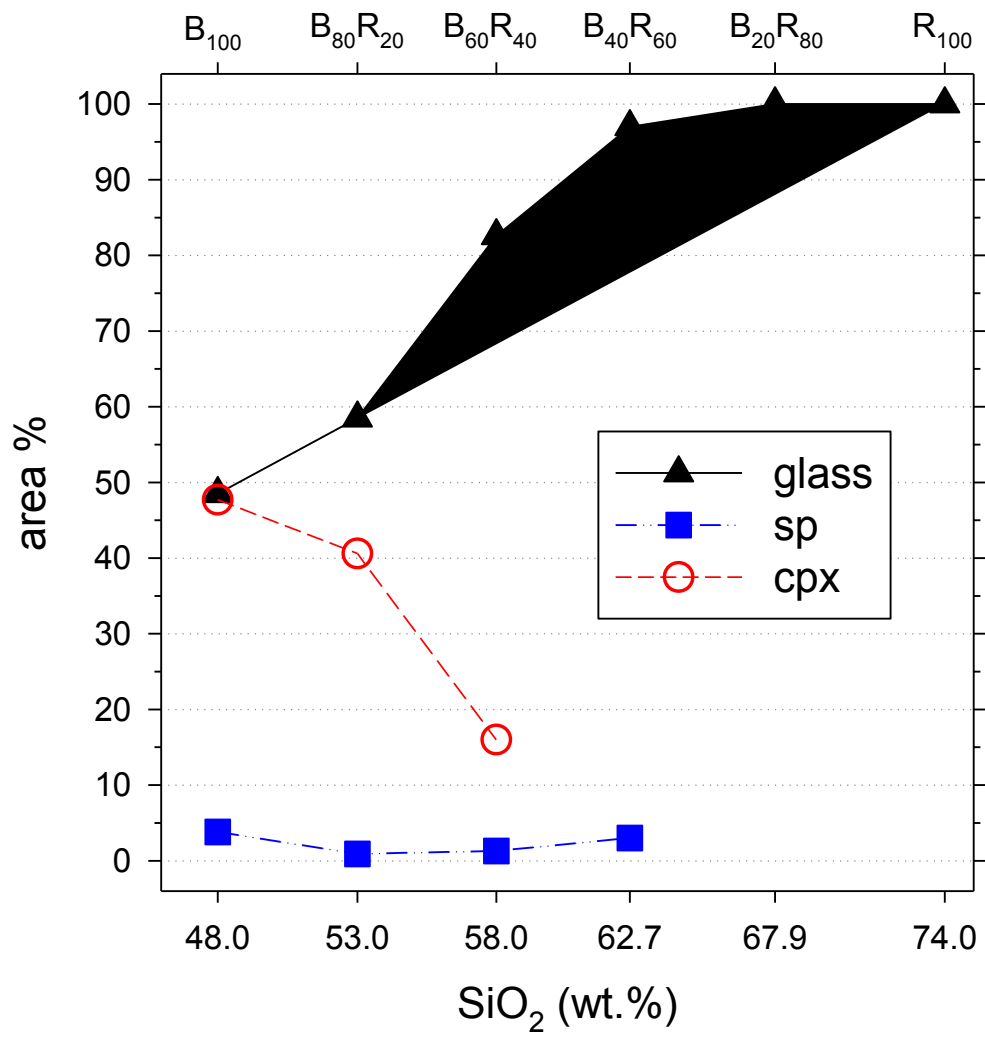


Figure 6

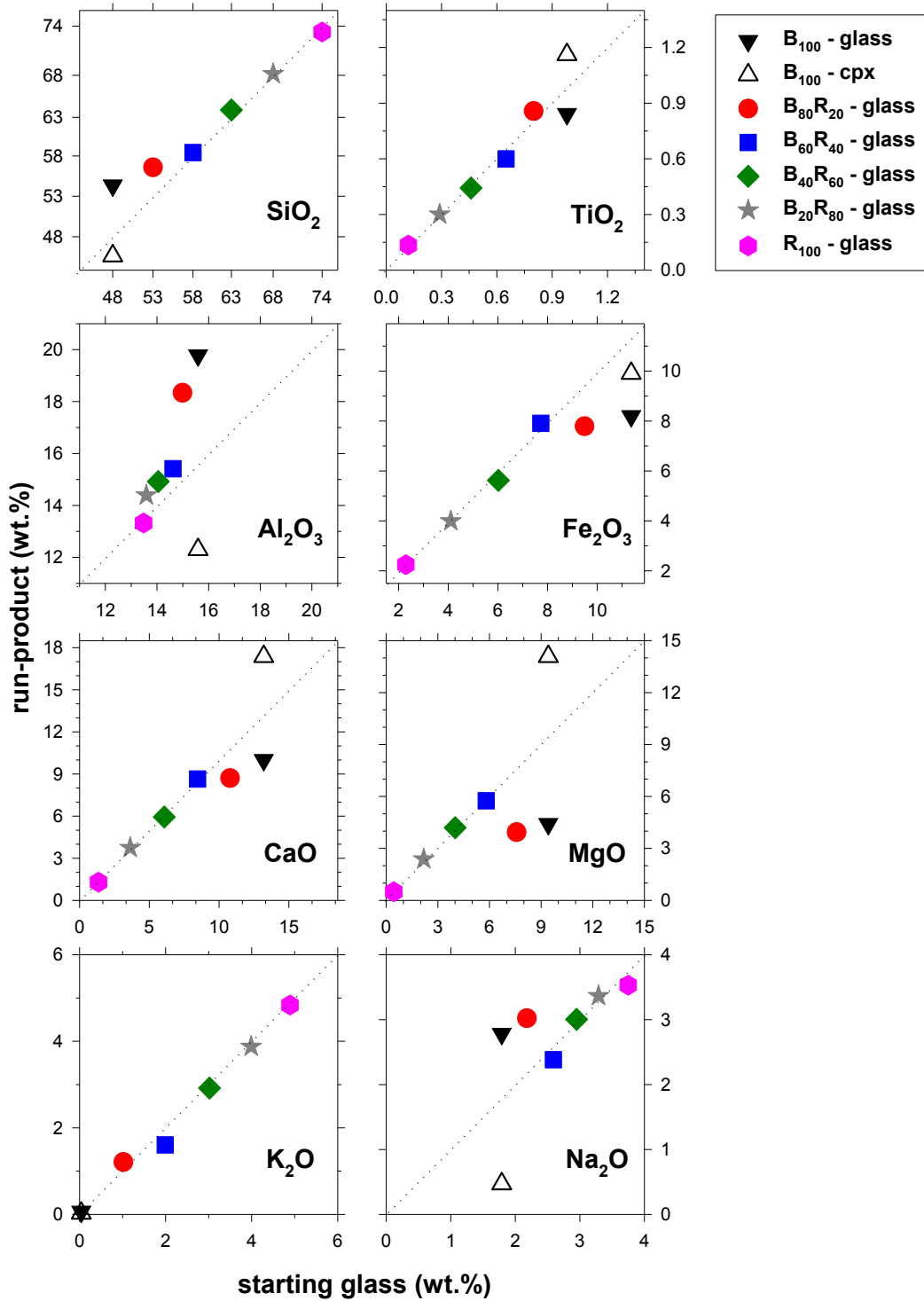


Figure 7

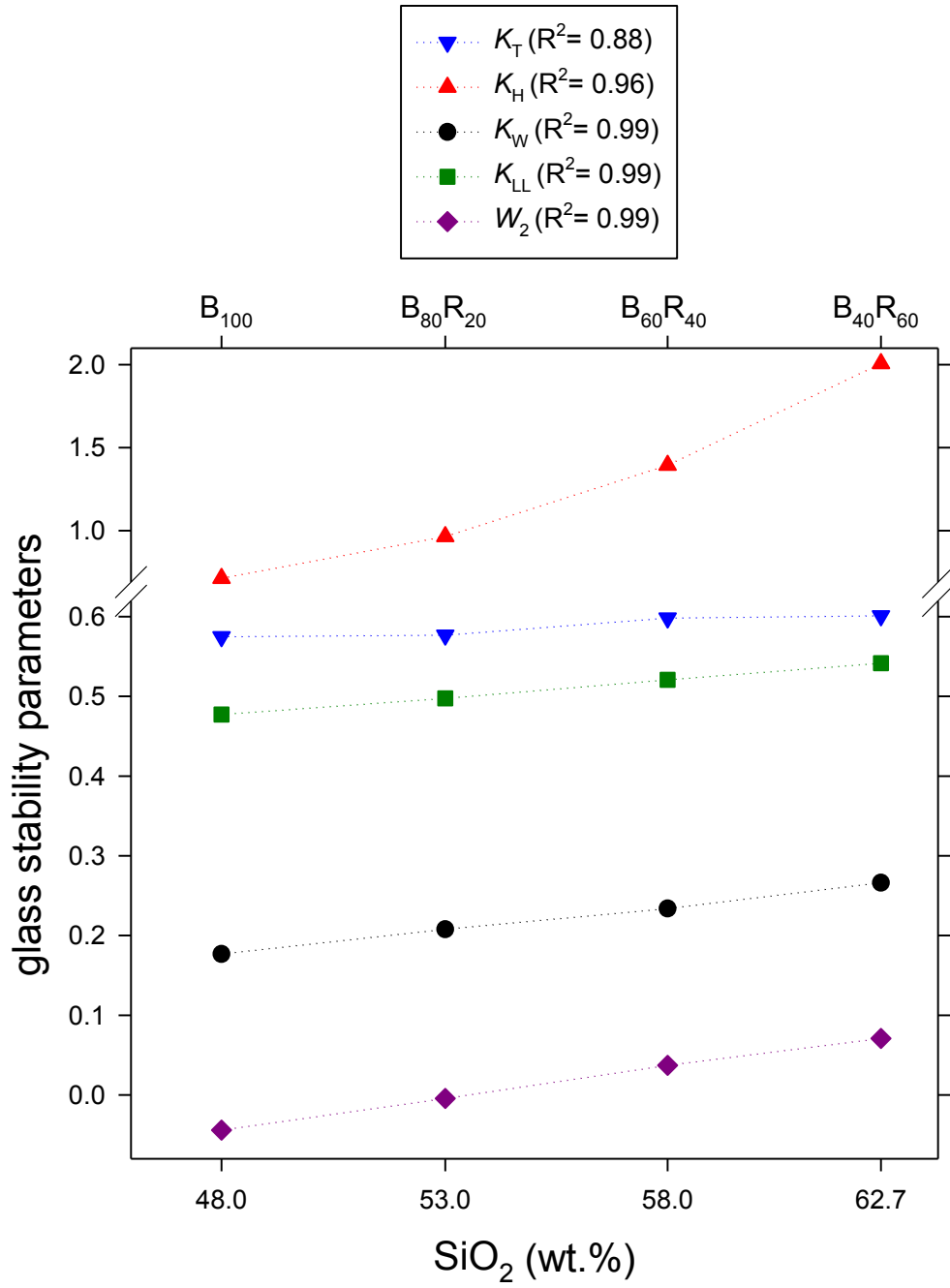


Figure 8

